



LAWRENCE
LIVERMORE
NATIONAL
LABORATORY

Dynamic Strength Increase of Plain Concrete from High Strain Rate Plasticity with Shear Dilation

W. Elmer VII, E. Taciroglu, L. D. McMichael

December 29, 2010

International Journal of Impact Engineering

Disclaimer

This document was prepared as an account of work sponsored by an agency of the United States government. Neither the United States government nor Lawrence Livermore National Security, LLC, nor any of their employees makes any warranty, expressed or implied, or assumes any legal liability or responsibility for the accuracy, completeness, or usefulness of any information, apparatus, product, or process disclosed, or represents that its use would not infringe privately owned rights. Reference herein to any specific commercial product, process, or service by trade name, trademark, manufacturer, or otherwise does not necessarily constitute or imply its endorsement, recommendation, or favoring by the United States government or Lawrence Livermore National Security, LLC. The views and opinions of authors expressed herein do not necessarily state or reflect those of the United States government or Lawrence Livermore National Security, LLC, and shall not be used for advertising or product endorsement purposes.

Dynamic Strength Increase of Plain Concrete from High Strain Rate Plasticity with Shear Dilation

William Elmer VII¹, Ertugrul Taciroglu², Larry McMichael¹

1: Engineering Technologies Division, Defense Systems Analysis Group: Lawrence Livermore National Laboratory. 7000 East Ave. L-126 Livermore, CA 94550

2: Civil & Env. Engineering Department, University of California, Los Angeles, CA 90095

Abstract

An increase in the strength of concrete when loaded dynamically has been noted in the testing literature since the early twentieth century. The origins or mechanisms leading to this increase, despite having been observed in a variety of tests, are not satisfactorily established. Aspects of test setup, specimen design, etc., have been shown to influence the outcome of any given test. More recently, computer representations of concrete have been tasked with analyzing or predicting the dynamic behavior of structures. Computers have also enabled an inward look at the same empirical tests, showing that some strength increase in compression can be captured by implementation of the proper plasticity model. The major factor touted for strength increase is the well known pressure sensitivity of concrete and a mechanism known as ‘inertial confinement.’ The present work proposes a new mechanism for dynamic strength increase, focusing on the failure mechanism of concrete in compression known as shear faulting. The faulting process and its associated plastic deformation mode is compared using several material models. Adjustments are made to some parameters within these models to study their effect on dynamic and inertial plastic response. Shear dilation, which does little to increase dynamic strength at moderate strain rates, is identified as a key component of a concrete material model subject to high strain rates. Shear dilation’s effects can be seen in the range of strain rates that are practically attainable in a laboratory by using the split Hopkinson pressure bar apparatus. They may also have an increasingly important effect on problems featuring even higher strain rates, such as blast, impact, and penetration through concrete slabs.

1. Introduction: Impact Pulse Testing

Two major review works firmly establish the existence of increasing compressive strength in a concrete specimen when an increasingly rapid application of load results in a higher strain rate to failure [2,24]. Both of these review articles contain data obtained using the split Hopkinson pressure bar (SHPB [14,17]) technique. The SHPB method is typically used to fill out the strain rate regime for which reliable and controlled laboratory data *for strength* is available. The ‘high’ strain rate regime is considered to be the two decades between 10^1 and 10^3s^{-1} . At these strain rates, strength at failure increases by a factor of two to three while strain at failure increases a modest 25-40%. Malvar *et al.* [24] cite the currently available sources of data and note that CEB [3] recommendations call for slightly more dynamic strength increase than the data might support.

Theories seeking to explain the strength increase center around several known explanations: increased microcracking and damage, inertial confinement of a pressure sensitive material, and geometric or frictional confinement effects. Of these, inertial confinement and geometric or frictional confinement effects have received the most amount of study. Furthermore, these two effects are conceptually the easiest to test in a computational study. Some additional references on these two effects will be made in §1.1.

The role of microcracking is likely the least well understood and the most difficult to model in a phenomenological manner. The role of cracking and crack branching is studied by Malvern [25–27] without establishing a direct link to strength increase. Experiments did conclude, especially through forensic post-test analysis [25], that specimens from high strain rate experiments exhibit a greater number of micro- and meso-cracks. These microcracks branch more frequently and take a more tortuous route through the matrix material *and* aggregates. Higher strain rates increase the cracking densities, which implies a larger amount of energy was absorbed. The connection to strength is then made by noting time delay phenomena [27] and increased area underneath the stress strain curve. However, it should be noted that increased crack density means increased formation of voids. Therefore, concrete has been observed gaining volume under applied shear, or dilating more under rapid application of load. Some computational material models account for dilation and thereby represent microcracking in a phenomenological sense.

1.1. Specimen Slenderness: Geometric and Boundary Condition Effects

In any conventional compression test, the specimen will eventually fail by splitting or fracture. This usually occurs along fracture planes or ‘shear faults.’ When the failure process is slowed down, microscopic cracks have time to coalesce and form in the same corridor, eventually forming a macroscopic crack. Bischoff [2] observed “an axial splitting failure [...] in specimens where frictional end-restraint was minimized, while the presence of end-restraint altered the crack pattern and caused an apparent shear failure, with the formation of cones at the ends of the specimen. Hakalehto [11] observed that, during dynamic testing, rock specimens were able to transmit more energy as the specimen length became shorter and the influence of the confining effect became greater.” Other observations made of more squat test cylinders indicate that the failure takes place due to many, slightly inclined longitudinal cracks.

1.1.1. *Boundary Conditions*

A unifying aspect of unconfined testing of brittle materials was mentioned above: the failure mode is always that of faulting on a cone of material confined on one side by the test apparatus. The angle made at the top of the cone depends on the frictional properties of the material *and* its interface with the test apparatus. Extraordinary steps are almost never taken to minimize friction in a dynamic test. Even if friction was eliminated, the test transitions to one more akin to a dynamic Brazilian test [32] (used for establishing the dynamic tensile strength) where a single crack splits the specimen in half lengthwise. Failure based on shear faulting, which results in two cones protruding from the test apparatus, is a hallmark of an unconfined compression test.

The failure process, as such, becomes subject to a number of geometric and frictional variations. The above quote acknowledges that more energy may be transmitted if the specimen length is shorter than its diameter and frictional confinement from the apparatus increases. Making the specimen more slender decreases the friction constraint with the apparatus while increasing the distance between shear cones. At extreme slenderness ratios, the failure mechanism transitions to a single angled shear failure ‘chopping’ the specimen in half.

1.1.2. *Inertial Confinement and Previous Computational Models*

Inertial confinement refers to the *elastic* process whereby rapid radial expansion due to the Poisson effect applies an inward force to the core of the compressed material. The effect also delivers a small increase in axial stress related solely to the specimen’s elastic properties and geometry. Forrestal [8] completes an in-depth mathematical treatment of radial inertia in the linear elastic regime. He concludes from the complete solution, as Kolsky [17] did using an energy approach, that the additional *axial* stress alone cannot fully explain the observed strength increase. Several authors, e.g. [2,19,29] *inter alios*, report that the separate but related phenomenon of rate induced, radial confining stress could potentially account for the observed strength increase. The inertial confinement phenomenon is quantitatively assessed in the exact elasticity solution, which shows an increase in rate induced, radial confining stress that is maximum at the core and decreases to zero at the boundary. However, unlike actual concrete specimens, the elasticity solution does not have a material strength limitation.

While the analyses within the linear elastic framework have provided a good basis for identifying some of the causes of strain-rate effects, they provide only a limited understanding of the strength increases observed experimentally. The key assumptions must encompass the entire range of material response—viz., through a framework where yielding is allowed and flow stress is pressure-dependent—since the notion of a stress state that applies specimen-wide is no longer descriptive when rapidly occurring plastic deformation accumulates locally. The admission of plasticity, and the subsequent lack of an exact solution, makes computational methods an attractive means to develop insight into the specimens response during the complicated evolution from a uniaxial stress state to a multi-axial stress state, e.g. [19,29].

In the realm of computational simulation, Georgin *et al* [9] apply a visco-plastic Drucker–Prager model to the compressive SHPB problem. This study does not model the apparatus and employs an axisymmetric model. There is no friction study as in [19], but the work considers fully fixed and frictionless end restraint conditions. They produce results

comparable to the testing literature by assuming that the true response lies between the two extremes. One unique contribution is a plot of the hardening variable for the fixed-end test, showing the formation of shear cones and a plastic localization zone at the core of the specimen. For the case of frictionless boundaries, the specimen deformation is badly non-uniform with respect to its length [29]. The deformation is indicative of a non-uniform stress state, which would violate the SHPB assumptions, but nevertheless may exist in experiments.

Specimen strength gain occurs in the laboratory regardless of whether it is a function of pointwise (material) strength gain or specimen level (mechanical) enhancements. Results and assertions that center on the question of material versus mechanical strength gain can be found in various literature focused on computation [18,19,31,34]. More recently Kim [16] compares J-2 plasticity and a pressure-dependant material in a simulated SHPB and concludes that rate dependence is entirely due to pressure sensitivity. Attribution of strength gain to inertial confinement persists in its Poisson-ratio-like form in many of the cited works, despite acknowledged axial non-uniformity of the plastic specimen deformation above the transition strain rate ($1 - 3 \text{ s}^{-1}$). Zhou's [35] model of aggregate at the mesoscale shows increased crack density, accompanied with strength gain, for higher strain rates. The natural treatment of dilation possessed by a mesoscale model that includes aggregate is further commented upon in §3.9. The 'natural' causes of strain rate strengthening effects, and their limits, are acknowledged in a research note from Magallanes [21]. The note advocates using only the strain rate curve multiplier in the portion *before* the transition strain rate mentioned in §1.2 and letting pressure sensitivity handle the strength increase at moderate strain rates. Previous simulation and modeling work has indicated a connection between pressure sensitivity, plastic flow and strength increase without a clear indication of the unifying mechanism.

1.2. Previous Investigations on the Role of Dilation

Janach [15] studied the role of bulking in the brittle failure of rocks. His experiments were not based on the typical SHPB and may have attained much higher strain rates than studied in this work for concrete. Janach stressed the point that failure cannot be separated from the loading process of brittle materials. The failure process can control the load history, necessitating an investigation of the failure mechanism and its effect on the load the specimen is transmitting.

Failure, or 'unloading' waves, are typically assumed to propagate from the radial periphery of the specimen toward the center with a fixed wave velocity c_f , which is much lower (by an order of magnitude) than the longitudinal wave speed in material that remains elastic [2,15]. Bischoff [2] notes that the experiments performed by Janach [15] were likely performed at strain rates in excess of 10^3 to 10^5 s^{-1} because of the test design. In Janach's test, a rock specimen was fired from a gas gun at a steel bar instrumented to measure stress. An accurate measure of strain rate was not available.

All inquiries made on the role of dilation in the dynamic strength increase share two characteristics: one, dilation is considered to be synonymous with unloading; two, dilation occurs on the outside of the specimen first, proceeding inward at the 'failure wave' speed, which is significantly slower than the elastic wave speed. The resulting delay and outwardly expanding material allow for confinement of the core material when 'failed'

and cracked material pushes inward on a still vital core. Crack growth is retarded within the core, sustaining stress and leading to increased small crack formation.

This phenomenon is fundamentally different than the elastic radial inertia caused by a Poisson effect, but may act in concert with it. More likely, radial inertia is responsible for moderate increases in strength at strain rates below the transition point ($1 - 3 \text{ s}^{-1}$) and the aforementioned type of shock-wave dilation is responsible at strain rates in excess of 10^3 s^{-1} . Intriguing and unexplained (from available literature) strength increase arises during concrete tests between these two extremes.

1.2.1. *Characteristics of Dilation*

Of these two previously mentioned characteristics that are associated with dilation, the first is especially at odds with the commonly accepted mechanism that causes dilation in concrete. Dilation, as opposed to simple volumetric strain, is necessarily created by shear stress. Inhomogeneous geomaterials dilate when shear stress drives aggregate closer and closer, until it has no choice but to ‘roll’ over the top of the nearest neighboring aggregate. Suggesting that dilation occurs on the exterior of the SHPB specimen because microcracking associated with failure begins there is partly inconsistent with the typical driver of dilation in computational material models; namely, activation of the yield surface causes plastic flow. The normal to this surface has a component in the positive volumetric direction because the material’s yield strength is sensitive to pressure. (Optionally, the plastic flow is partly or wholly non-associative.) Dilation does not occur on the exterior of the specimen if it is unloading because there is no imbalance in principal stress that would be needed to ‘yield’ the material and drive plastic volume change.

Janach recognizes the latter point on dilation as an idealization and comments on the regime of loading still left unexplained. At the extremely high strain rates estimated for his experiments, it may be possible to make the assumption that an unloading wave propagates into the interior normal to the outer surface of the specimen. For SHPB tests, multiple reflections occur within the specimen before the failure process initiates. The effect of “bulking and frictional losses” is therefore to slow the failure process of the ‘jacket’ concrete around the core of the specimen. The dilation within the typical SHPB specimen, however, is truly driven by shear stress and initiates on planes with a much larger angle to the sides of the specimen. These planes are in fact those of the shear cone interfaces with the test apparatus.

1.2.2. *Goal of the Present Work*

The present work seeks to model the split Hopkinson pressure bar test on concrete with a high level of fidelity and evaluate many different material models for suitability in reproducing dynamic strength increase. Dynamic strength increase factors (DIFs) are gathered here as they are in the actual test, by measuring the intensity of stress pulses in the test apparatus (described in §1.3). Two simulation codes with unique material model types are compared. Four independent material models and several modifications of those models are tested in the nonlinear hydrocode ALE3D [1]. All ALE3D simulations are fully Lagrange for the purpose of this work. In addition, four separate material models are tested in the explicit dynamics code DYNA3D [20]. One model, the K&C model described in §2.1, is shared between both of these codes. While the implementations are similar, they are not exactly the same. However, benchmark studies are performed in this

work to show that both codes predict similar dynamic behavior for concrete specimens represented by that class of phenomenological plasticity.

Furthermore, this study seeks to shed light on the actual mechanism at work in producing dynamic strength increase in test specimens. The inclusion of certain effects that occur only during plastic flow at high strain rate will shed light on the mechanism at work in real world tests. Not only do computational representations of these tests allow a look inside the specimen at a fine time scale, but the accuracy and assumptions about various phenomena manifest themselves in the pseudocolor images of the results produced.

1.3. Simulated Experiment Test Setup and Data Collection

Simulations of a truncated version of the SHPBs typically seen in a lab are introduced here to study dynamic increase. The incident and receiver bars are shortened so that little computational time is lost in the propagation of waves in an elastic media. The test setup consists of an incident and receiver bar, both plain steel 105 in long, sandwiching a test specimen with a height and diameter of 2.05 in. All steel bars, incident receiver and striker, are made of the same material and are the same radius as the specimen. The incident bar is impacted with a striker bar, length 30 in, which has a variable velocity shown in Table 1. The format of Table 1 (two rows, seven columns) will be used later to present figures from the tests performed at each impact velocity.

Table 1
Striker bar impact velocities.

Striker velocity (in/s)	100	140	170	200	250	300	320
	380	410	435	460	510	560	600

Data is collected in a very similar manner to experiments. Instead of placing virtual strain gages on the exterior of each bar by monitoring the strain in a single element, the average stress through the bar cross section is measured. Because the stress is averaged through the entire cross section, variations in pulse intensity between the core and the bar surface are smoothed. In ALE3D, a single layer of elements at the midpoint of incident and receiver bars is averaged to get bar stress. In DYNA3D, tied slide surfaces are used to monitor the total force across these midpoints and force is converted to stress. Stress is converted to strain using a simple one dimensional assumption. According to SHPB theory, the specimen stress, strain and strain rate is recovered from the strain signals according to equation 1.1;

$$\epsilon_s = \frac{2c_o}{L} \int_0^t \epsilon_r dt, \quad \dot{\epsilon}_s = \frac{2c_o}{L} \epsilon_r, \quad \sigma_s = \frac{EA}{A_s} \epsilon_t \quad (1.1)$$

where ϵ_r, ϵ_t are the reflected and transmitted strain pulses measured in the incident and receiver bars, respectively. Stress is converted to strain for use in equations 1.1 by assuming a uniaxial linear elastic relationship $\sigma = E\epsilon$. Friction between the bars and the specimen is consistently modeled with a static coefficient $\mu = 0.2$ across all code platforms. The theoretical value of wave speed $c_o = 180,215$ (in/s) is used, based on the bulk modulus and density of the material. Experimentalists will often measure this value. L is the length of the specimen and σ_s is simply gathered from the signal in the

receiver bar, as there is no difference between the bar area A and area of the specimen A_s .

2. Material Models and Simulation Codes

Much work has been done dealing with material model formulation and behavior. Implementation of these techniques into fast running simulation codes has preceded this study by many years. This section will highlight some of the relevant details of each material model under consideration and couch that behavior into one of several points of interest: pressure sensitivity, bulk response to shear load, and damage behavior. Tu [33] evaluates some models similar to the ones under study here. Information about all ALE3D materials can be found in volume 2 of the ALE3D users manual [1]. An in-depth study of concrete models in DYNA3D can be found in Noble [28]. Cap model formulation and fitted parameters are available in Simo [30].

All of the material models studied here incorporate some type of pressure dependence. The pressure dependence is not equal between models and each method handles and calibrates this dependence in its own way. No effort was made to classify the fit to a ‘correct’ concrete. Furthermore, since this study is interested in only dynamic *increase* factors, no effort was made to equilibrate yield strengths in unconfined compression. In fact, several different ‘strengths’ (variations of material parameters for the same constitutive formulation) are studied in later sections.

Most of the discussion to follow will focus on the K&C model presented later in §2.1 because it is roughly equivalent in both codes. DYNA3D material models will be referred to by number because it is the clearest way to convey the material model details. For further information, see the manual [20].

The model of secondary interest in ALE3D is called ‘porous crush’ and is governed by a simple strength model and an equation of state that are both based on tabulated data. The model assumes a density of the solid material ρ_s that is recovered when porosity ϕ is crushed out (zero). Damage in the model evolves with compressive stress and equivalent plastic strain, as well as tensile principal stresses and pressure. Damaged and initial material states share a common equation of state, except for damaged material subject to a tensile applied pressure. Details of the model are left to [1].

The Holmquist–Johnson–Cook (HJC) model incorporates pressure dependence and strain rate dependence in the same equation. σ^* is defined as a normalized failure stress $\sigma^* = (\sigma/f'_c)$, and equated, as shown in Equation. 2.1, to a series of material constants, the pressure and the strain rate:

$$\sigma^* = [A(1 - D) + BP^{*N}] [1 - c \ln(\dot{\epsilon}^*)] \quad (2.1)$$

where each starred value is normalized in turn. Damage accumulates in proportion to plastic strain, but unlike other concrete and geologic constitutive formulations available in DYNA3D (e.g., material types 16 and 25), it can be attributed to volumetric as well as deviatoric components of plastic strain. This feature makes the model increase its damage to fracture (total failure) under increased confining pressure, thereby increasing a hypothetical structure’s ductility if confined. A plot of σ^* versus P^* shows an initial slope up to a point where a cutoff value called SMAX is reached. Also, this plot must be made with a consideration for damaged versus undamaged material. At full damage, the

cohesion represented by the A parameter is gone and the material will not carry shear stress without applied pressure.

That elimination of cohesion is very similar to another material we study in DYNA3D, material number 16 [12], or a generic type of ‘pressure dependant yield.’ Material 16’s yield surface is given by Equation 2.2. While the HJC model is more like a Mohr–Coulomb with Tresca limit type bilinear yield (which material 16 can also model), we choose to use material 16 in such a way that pressure dependence is accomplished by two smooth curves describing the yield strength of intact and failed material.

$$\begin{aligned}\sigma_y &= a_0 + \frac{p}{a_1 + a_2 p} \quad (\text{intact}) \\ \sigma_y &= a_{0f} + \frac{p}{a_{1f} + a_{2f} p} \quad (\text{failed})\end{aligned}\tag{2.2}$$

Material 45 in DYNA3D is very similar to this formulation, except that the yield surface description includes three such curves to describe initial, peak strength and residual pressure dependence. The difference from the HJC model comes when the damage like (λ) variable is looked up in a table to obtain a scaling parameter between yield curves ($\eta(\lambda) \in [0, 1]$). This allows greater control over the transition from a cohesive material to one that has failed. We will entertain two versions of this relationship, one with a very short damage cutoff (plastic region) and one where damage is allowed to evolve over a wider range of equivalent plastic strain.

The aforementioned methods share the properties that, when the yield surface is active and the material is not fully damaged, associative flow dictates volumetric strain occur as a result of shear stress. The normal to all of these surfaces points up *and back* in pressure–deviatoric stress space, indicating a positive plastic bulk strain will occur. This effect in each of the aforementioned material models, however, does not last forever. The flow rules for each material will be commented on in later sections.

Another material in DYNA3D studied here, material type 25, will also dilate as long as its yield surface is active and it is not subjected to high pressure. Dilation will cease when kinematic processes have contracted the *mobile* cap surface (with the correct input option) and the stress point lies at the intersection of the cap and failure surfaces. Shrinking volume due to shear stress induced plasticity (crushing) is captured if the cap is active at high pressure. Further details of the model can be found in [20].

2.1. *K&C Concrete Model in ALE3D and DYNA3D*

DYNA3D material type 45 and K&C model (type 65) are very similar. The K&C model is capable of creating all of the material parameters it needs from a single unconfined compressive strength. Crawford and Malvar provide some feedback about this model [5,22]. Details are also covered by Malvar [23], but the literature does not contain a robust distinction between DYNA3D materials 45 and 65. The adjustments to material 65 are subtle and were implemented based on the developers’ experience using the code.

The ALE3D K&C model is very similar to DYNA3D K&C and type 45, with information about its differences found in the ALE3D material manual. Additional details can be found in Noble [28]. All three models start with the same three failure meridians, which relate the allowable difference in principal stress to pressure and are defined by a set of parameters fitted to triaxial test data. Parameters for three sets of equations similar to

equation 2.2 are input, except a_{0f} is assumed zero. Using three equations and a tensile pressure cutoff eliminates the need for a_{0f} .

A significant scaling of the yield curves based on this third invariant is introduced. Three invariant models mimic the increase in failure stress when two out of the three principal stresses are balanced with one another. The third deviator stress then needs to be larger than normal to cause failure. The effect washes out with increasing pressure.

Damage evolution rules incorporate lambda stretching and different exponents b_1, b_2 to delineate damage occurring under tensile or compressive pressure. The effective plastic strain definition remains the same, but the incremental damage $d\lambda$ in ALE3D is slightly different than the DYNA3D K&C model, in that $f_t = 1.58f_{\text{comp}}^{\frac{2}{3}}$ according to CEB recommendations, which decouples the damage under confining pressure from the tension meridian and instead uses compression data. This behavior can be adjusted in material 45 by a suitable choice of f_{tens} .

2.1.1. Dilation Treatment in ALE3D and DYNA3D

Dilation would normally take place as a natural byproduct of associative flow for each of the K&C models. This behavior is so readily associated with a physical mechanism that it receives special algorithmic treatment. In real geomaterials, dilation will increase only to the point when aggregates have separated a suitable amount and continued shear stress would tend to drive a contraction. The material models under consideration do not model the dilation *and* contraction, but instead *limit* dilation during loading in some way. Dilation is typically limited by tying its evolution to the damage process or limiting the amount of volumetric plastic flow. Both options produce a non-associative flow rule that becomes increasingly less associative as the material deforms and/or damages.

Dilation can *optionally* be slowed and stopped by damage in both DYNA3D and ALE3D material models, as shown in equation 2.3,

$$\Delta\epsilon_{\text{vs}} = \Delta\epsilon_{\text{in}}\omega\frac{\partial\bar{\sigma}}{\partial p}, \quad \omega = \begin{cases} \lambda < \lambda_M & \omega_0 \\ \lambda \geq \lambda_M & \omega_0\eta^m \end{cases} \quad (2.3)$$

where $\Delta\epsilon_{\text{in}}$ is the inelastic strain increment and m is an exponent on the damage parameter η that allows dilation shutoff. ω_0 is the initial dilation value, which has some experimental basis (covered in §2.3 and §7.1–7.2 of [5]) and is discussed in this work in §3.7 and Table 4. DYNA3D material 45 also evolves dilation in the fashion of equation 2.3.

An important detail of the ALE3D model to be showcased later is the availability of the dilation strain as an output in the plot files. Since the strain takes place due to yielding from shear stress, it is linked to “rubble formation” in the material. Aggregate will ‘roll’ over adjacent aggregate, gaining porosity but crushing matrix material (cement) in the process. Volume change due to shear can indicate more about the physical phenomena the material model is intending to match than can simple ‘damage.’ For DYNA3D, a visualization of dilation needs to rely on equivalent plastic strain or principal shear strain to infer that dilation took place in the material.

Likely the most significant difference between the K&C model and material 45 in DYNA3D, for dynamic plastic processes, is the decay of the plastic flow that causes dilation. For the implementation in DYNA3D, the dilation is reduced by a denominator

that grows with additional volumetric strain. Again the dilation decrease parameter m is used (§6.5 of [5]):

$$\omega = \frac{\omega_0}{\cosh(m \epsilon_v)}, \quad \epsilon_v = \ln V \quad (2.4)$$

where V is the relative volume of the element. Equation 2.4 *lacks* a cutoff based on the damage variable η . Furthermore, the dilation component is not reduced when compressive volumetric strains are present.

The difference in formulation also has an effect on the evolution of damage. Since dilation affects the volumetric strain, it in turn affects calculation of the damage increment $d\lambda$. Treatments in DYNA3D and ALE3D contain some increment of plastic strain that is affected by how dilation is slowed or stopped. Both the decay in the associativity of the flow rule and the amount of equivalent plastic strain that causes damage (migration between yield curves) can feed back into damage evolution and possibly play a significant role in dynamic strength increase.

The damage parameter λ and the closely related ‘delta ratio,’ which is equal to 1.0 at the maximum failure envelope and approaches 2.0 as the strength degrades, can accumulate in a variety of ways. Dilation must be a response to shear stress, rather than to pure volumetric crushing or tensile damage. Retarding the decrease in dilation causes a decrease in the damage increment and overall damage occurs more slowly. Eventually, however, both plasticity laws will show a complete loss of strength.

In a highly dynamic environment, the presence of large dilation strains indicates that a large amount of stress was carried for a short period of time (before damage was able to turn it off). Large dilation strains indicate a loading scenario where aggregate has been separated violently from the mortar. Subsequent confining pressure on a (real world, but not simulated) concrete specimen in such a state will likely not have the same strengthening effect. We shall show the accumulation of dilation occurring at high strain rates can greatly exceed that seen in a quasi-static test, even if the exponent in equation 2.3, m , is equal to unity. Also, we will explore the role that this dilation plays in the dynamic strength increase of a SHPB specimen and test a variety of inputs to the various material laws presented.

3. Simulation of Concrete Subject to Unconfined Compression Impulse

This section covers the specimen design, static strength calibration, and simulation of split Hopkinson pressure bar tests. Dynamic results are culled from virtual SHPB ‘strain gage’ time histories. The peaks of those time histories comprise the DIF and provide a time at which to take a very detailed look inside the specimen and at the plastic processes occurring during dynamic failure. It will be shown that even for a phenomenological model the stress, strain and strain rates are inhomogeneous throughout the specimen and that the conventional DIF is the result of considerable averaging of spatial and temporal non-uniformity. It will be shown that the strain rates observed in individual elements do not correspond to the strain rate calculated by the SHPB theory given in Equation 1.1 and vary widely within the specimen. Furthermore, evidence of shear faulting and dilation occurring on those faults, which contributes to strength gain, is presented.

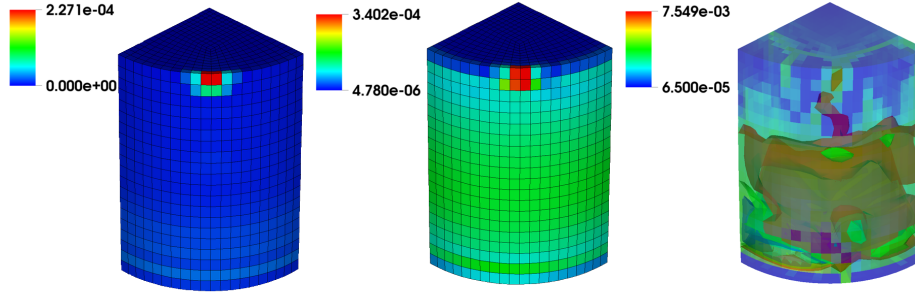


Fig. 1. An anomaly in the damage parameter λ from a mesh artifact is shown early (left), later (center) and in the interior (right) for the high strain rate test specimen of K&C material.

3.1. Specimen Mesh Geometry

At first, the starting specimen quarter-round geometries were meshed using a simple butterfly mesh. Some attention was paid to the proportion and distribution of elements between the square core of the quarter-circle cross section and the outer layers of the mesh where the butterfly is merged. Despite these precautions, some artifacts related to the choice of a butterfly mesh were later discovered in the results. The internal ALE3D mesh generator [1] was used to create the butterfly mesh of the specimen and the incident and receiver bars. The specimen was much more finely meshed in the longitudinal direction than incident and receiver bars.

A mesh artifact was discovered in this approach, which led to an artificial damage concentration and necessitated a change in the way the specimen was meshed. The flaw was noticed for simulations using the K&C material. Figure 1 shows the damage distribution from the highest speed impact of 600 (in/s) and the original manner in which the specimen was meshed. The damage parameter λ is shown in both pseudo-color and contour plot types. Figure 1 shows a hot spot of damage that can be attributed to the mesh. It appears at the interface of the receiver bar and the specimen (the receiver bar, above, has been removed for clarity). This is the location in the mesh where two block structured portions are glued together to form the ‘butterfly,’ as is common when projecting block-structured finite elements to a cylinder. The anomaly shows up in both early time (left) as the impulse begins to reflect between receiver and incident bar and build stress in the specimen, and later (center) when damage has begun spreading throughout the length. This abnormally high level of damage skews the strength properties locally and on a system level. The final subplot shows damage (right) at an even later time (about 10 μ s) after the peak strength. A single set of elements connects the anomalous region on the surface to the more highly damaged core with a red flame like contour.

In light of this development, a newer mesh was adopted that seeks to surround the outer portion of the specimen in a smooth layer of elements. Butterfly seams in the mesh are moved much closer to the core. A transition layer of elements is used to get an effective level of mesh refinement at the outer periphery. The new specimen design can be seen in Figure 2 with the same damage variable evolving in a more natural way (upper row). The upper right subplot displays no ‘flame’ contour extending upward and the boundary of the specimen remains free of mesh artifacts (upper left). Damage and dilation are shown

on the lower two subplots, left and right respectively. Strength *trends* later observed in §3.4 were only mildly affected by this anomaly. Average element volume in the newly adopted specimen is about $2.44 \times 10^{-4} \text{in}^3$ and mesh refinement studies are omitted here (but have shown little effect on the results, due to the compressive loading environment [6]). Results presented in §3.7 would have been affected if the butterfly mesh artifact had been allowed to remain. A profile of the interior of the specimen is also shown on the

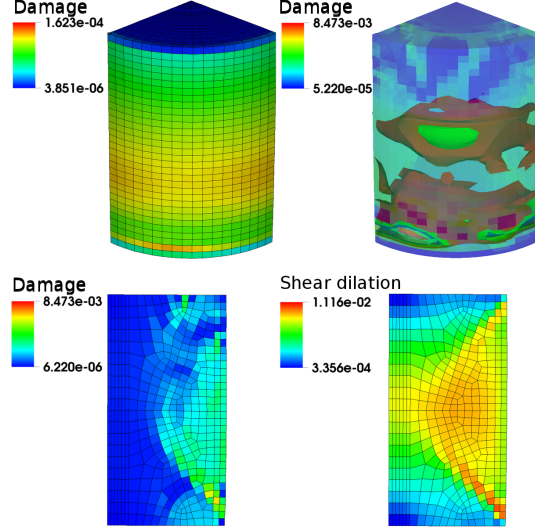


Fig. 2. A corrected mesh (upper row) eliminates the anomaly in the damage parameter λ for the new specimen type, suited for the detection of shear dilation (lower right) strain at high strain rate using the K&C material.

bottom row of Figure 2. The lower left plot is of damage, and the lower right shows shear dilation at a time slightly after peak strength. Various material models' dilation response will be discussed in depth in §3.7.

3.2. Material Names and Types Studied

The names assigned to the different material models are shown in Table 2. This list represents the first set of models under discussion in this work. Each model is pressure sensitive and some contain variations on the concrete strength. Note that Table 2 also indicates which simulation code was used for a given material type.

3.3. Quasi-Static Simulation and Typical Failure Modes

Static calibration tests were carried out on the various material models. The tests are not exactly 'static' since they were performed in an explicit code over the relatively short time of 0.05 seconds. The tests were displacement controlled to a strain between 0.7-2.0%. Figure 3 shows HJC Concrete 7000 with the largest peak stress and the porous

Table 2
Material Model Names and Descriptions

Material Model Tag	Material Model Description
KC5500	K&C ALE3D model, calibrated for $f'_c = 5500$ psi
KC4000	K&C ALE3D model, calibrated for $f'_c = 4000$ psi
KC3000	K&C ALE3D model, calibrated for $f'_c = 3000$ psi
PC5500	Porous crush ALE3D model, calibrated for $f'_c = 5500$ psi
PC3400	Porous crush ALE3D model, calibrated for $f'_c = 3400$ psi, less extensive strain rate dependency curve
HJC Concrete 7000	Holmquist–Johnson–Cook model, calibrated for $f'_c = 7000$ psi
DYNA–MAT16	Pressure dependant yield model, DYNA3D material type 16.
DYNA–MAT25 CAP	Cap plasticity model, DYNA3D material type 25.
DYNA–MAT45	Three curve pressure dependant yield model, DYNA3D material type 45.
DYNA–K&C	K&C model, calibrated for $f'_c = 4000$, DYNA3D material type 65.

crush model PC3400 with the lowest. The four DYNA3D models have a higher initial slope and a lower ultimate strength than the ALE3D models generally have.

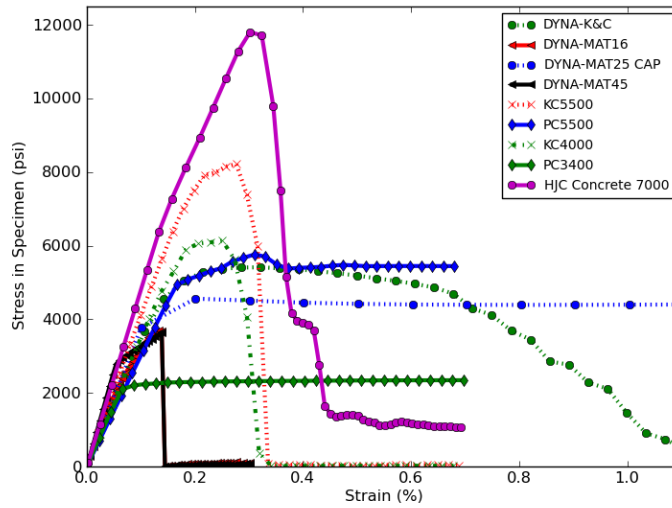


Fig. 3. Quasi-static tests conducted in 0.05 seconds to a strain of at least 0.7%

Several models do not soften, including the DYNA–CAP model and both porous crush models. Damage has been built into the porous crush, but is not activated under these entirely compressive loading regimes. The backbone curves are plotted here for the sake of illustrating some differences in the particular models. Only the peak strength is of real interest, since it alone is used as a baseline for the dynamic tests to follow.

Static tests feature very similar boundary conditions as the dynamic impact tests. The specimen was sandwiched between two steel plates, interface friction coefficient of

$\mu = 0.2$, on top of which the displacement was prescribed. Testing the specimen in frictional contact with steel removes any of the ‘structural’ strength effects related to the test apparatus from the dynamic test. Several of the materials under consideration have the ability to carry additional confining pressures into the core concrete, raising the effective strength of the material in this region. This can be seen in the generally higher strength values of Figure 3 than what the materials were supposedly calibrated for. Figure 3 underscores the importance of conducting multi element tests with realistic boundary conditions in order to classify material model behavior.

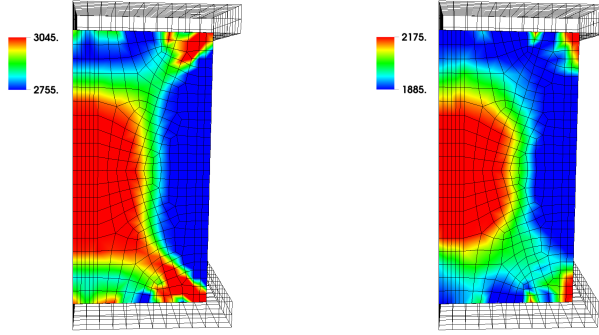


Fig. 4. Pressure in the characteristic X shape for the KC5500 material (left, min=2755 psi, max=3045 psi) and the PC5500 material (right, min=1885 psi, max=2175 psi)

Figure 4 shows the structural confinement phenomenon for K&C and porous crush concrete whereby additional confining pressure is collected from the concrete and steel interface and transferred to the core. The symmetry plane of the concrete is facing the viewer, and pressures in the steel are not plotted, which makes the steel mesh appear empty. Tight bounds on pressure were chosen for each case represented in the left and right subplots to highlight the pressure transfer. Confining stresses develop at the radial periphery of the specimen near the friction interface with the steel. This pressure is carried inward along a path that is roughly X shaped when viewed from the side, but is really the three dimensional shape of two frustums joined at the smaller diameter. The porous crush model shows a lower core pressure, which correlates well to its lower yield strength.

3.4. *Dynamic Increase Factor Results*

This section covers the dynamic strength increase seen in computational material test specimens. The data reduction process for dynamic tests gives pairs of peak specimen stress and accompanying strain rate. Strain rate increases monotonically with higher striker bar impact velocity. Figure 5 shows the computational results, with some experimental data incorporated as a scatter plot for reference. The first notable feature of Figure 5 is the ease at which the computational materials attain large strain rates. The strain rate, recalled from equation 1.1, is directly proportional to the reflected stress. With limited exceptions, simulated specimens have little trouble reflecting nearly all input stress. The boundary between the incident bar and specimen approximates a free

surface at high striker impact velocities, causing the pulse to invert. Again, the strain rate information is collected at the same instant as peak stress is attained. Material KC4000 seems to have a lower strain rate, absorbing more of the incident pulse at the instant when the specimen is displaying maximum stress carrying capacity.

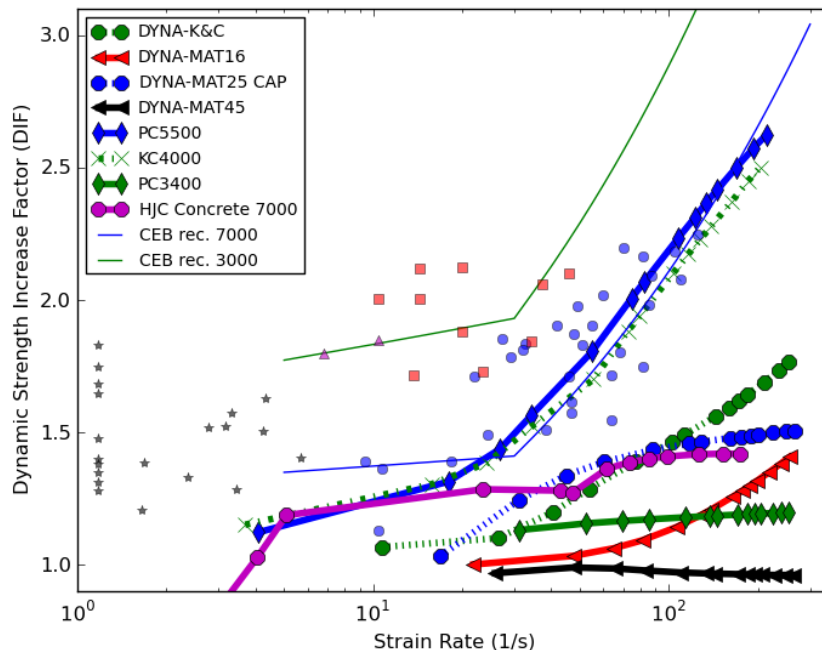


Fig. 5. Predicted DIF factors from concrete models in ALE3D and DYNA3D, some experimental data is shown from [2]

The simulated strain rate values end up well beyond those typically attained in the real life tests that the SHPB simulations were patterned after. The raw signals from several tests were patched together to visualize why reflected stresses are so large. Reflected stress arrives at the incident bar measurement point at the same time the transmitted stress is measured in the receiver. Figure 6 shows an abbreviated version of the receiver bar stress and the reflected stress (inverted).

Follansbee [7] offers a correction to so called Pochhammer–Chree [4] oscillations that is not adopted in this work. This and other limitations on the measurement of bar wave speed suggest that traces in Figure 5 should be shifted to a lower strain rate. Although none of these corrections are performed, this would put the abscissas of the experimental data more in line with what has been observed.

Note the lack of softening response for porous crush models displayed in Figure 6. Both porous crush models display a flat tabletop pulse with some of the aforementioned oscillations in the transmitted signal. The height of this transmitted signal increases for PC5500, but not for the weaker version. (The strength increase is dwarfed by the increase

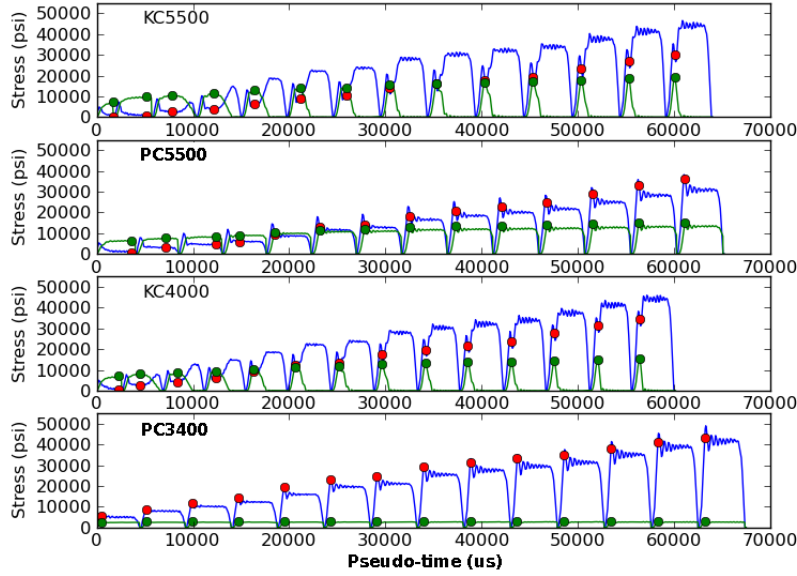


Fig. 6. Peak signals patched together from select ALE3D materials. Green trace is the transmitted signal, blue is reflected (inverted for clarity). Green dots indicate stresses used for DIF, red dots are used to calculate strain rate.

in input pulse amplitude.) Even though the specimen has a long time and lots of strain accumulating during which it could potentially gain strength, PC3400 does not do so.

For PC5500, the fact that the peak transmitted strain moves from the later portion of the pulse to the earlier point (the green dot moves to the left side) indicates that the mechanical impedance of the specimen decreases at very high strain rates. The incident bar to specimen interface is moving almost independently of the receiver interface. Reflected stress values are likely too large to accurately model the real system, even though in some cases a larger and larger pulse is being transmitted. The incident bar to specimen interface acts almost like a free surface of the incident bar, reflecting the mirror image of all the input energy. This is an issue displayed by several of the computational materials as the strain rate increases past the first five or six bar impact velocities studied here.

3.5. Dynamic Strength Increase Trends

The strength trends displayed in Figure 5 are much more significant than the differences in strain rate. Materials that include a rate enhancement table, unmodified K&C models and PC5500, gain *more* strength at the highest strain rates than has been observed in the empirical data plotted. The most interesting behavior is displayed by those materials *not* gaining strength at increasing strain rates. DYNA-MAT45 starts with a strength gain of about 10%, but gives back 5% and actually *weakens* below the static strength. DYNA-MAT45 in this plot has a very brittle damage curve, and changes to this behavior will be considered in §3.8.

Table 3
Material Model Variations

Material Model Tag	Material Model Description
KC5500 no rate	K&C ALE3D model, $f'_c = 5500$ psi, rate table turned off
KC4000 no rate	K&C ALE3D model, $f'_c = 4000$ psi, rate table turned off
KC3000 no rate	K&C ALE3D model, $f'_c = 3000$ psi, rate table turned off

Materials without strength gain are *still sensitive to pressure*. Their yield strength is a function of confining pressure and should be subject to strength gain from inertial confinement. It can be concluded immediately that increased core pressure, assumed to be provided in increasing amounts by inertial confinement, is not the only factor in strength gain.

The two porous crush models, PC3400 and PC5500, are both similarly sensitive to pressure. However, only PC5500 has an extensive strain rate table that drives its sensitivity to strain rate. The tabular strain rate multiplier for the initial yield of PC5500 can get as high as 5.0 in compression, while PC3400 is limited to 1.4. The model does not contain any other algorithmic mechanisms (e.g., an associative flow rule) that help it gain strength.

PC3400 features a nearly flat response; its strain rate table was tuned to a specific experiment and the tabulated pressure sensitivity does not contribute additional strength enhancement (from potential inertial confinement effects). Similarly, the DIF of HJC concrete flattens out. The HJC model has only one parameter to adopt itself to strain rate sensitivity and seems to saturate at a DIF around 1.4.

3.6. Rate Table Enhancement for K&C materials in ALE3D

A simple experiment can be performed where the rate table enhancement for K&C materials in ALE3D is turned off. The modified material names are listed for reference in Table 3 and the DIF is plotted in Figure 7. The ‘no rate’ *static* strengths were used to normalize both curves in this figure because the supposedly ‘static’ curves show some influence from strain rate effects (mild inertial confinement). K&C material models with and without the strain rate table enhancement show an effective reproduction of an experimentally observed fact: lower strength concrete displays a tendency to gain more strength when loaded rapidly than high strength concrete. The three materials utilize the exact same rate table and tabulated λ — η values, but differences in their pressure dependant yield parameters (and therefore plastic flow properties) work to increase the DIF as static strength is decreased. The effective mechanism separating the DIF for these materials becomes more pronounced at very high strain rates. This is the case whether the rate table is turned on or not.

Figure 7 shows that the strength increase from *plastic processes alone* matches up well with the strength level given by available data. In other words, the data and the simulation would match well if the simulation curves were shifted to the left by a half decade. Section 3.10 provides further evidence why strain rates reported by SHPB tests should not be used in judging FEM effective rates of strain.

The strength increase with rate enhancement falls within the CEB guidelines (shown in solid lines), but the validity of these guidelines when they are extended to very high

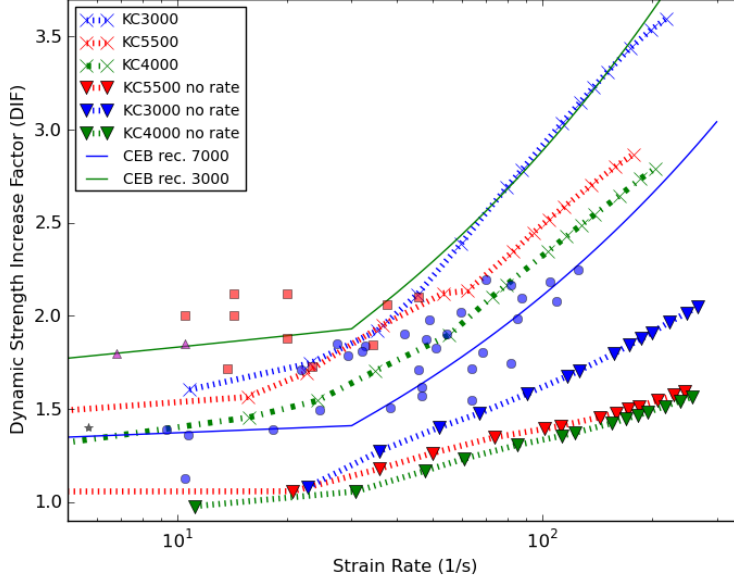


Fig. 7. K&C Model DIFs for variations of f'_c . Models with the rate table use the baseline static strength from the corresponding strength without a table. Thin lines are CEB recommended values for 3.2 (upper) and 7 ksi (lower) concrete.

strain rates has been questioned. Since the strength enhancement is a product of strain rate tables *and* dynamic plastic processes, it will be difficult to predict for a general structure when dynamics, rate enhancement, or both are contributing to strength gain.

Rate enhancement occurs at moderate strain rates as well. The difference between the strength displayed in ‘quasi-static’ tests for materials with a rate table versus those without, average 23.8% among the three K&C models. If these are removed from the static baseline (the ‘no rate’ static strength is used in Figure 7) the DIF values reach to an unreasonable strength regime, with the weakest concrete, KC3000, gaining 3.5 times its static strength. Grote [10], in a modern work, cites DIFs of 3.0 and above, but only for very small samples containing mortar alone. Grote’s work can be misinterpreted as evidence of very large DIFs in concrete.

3.7. Dynamic Strength Increase and Dilation

Figure 7 has shown that strain rate effects were not entirely removed from the static test. Focusing on a single concrete strength, $f'_c = 5500$ for the K&C model in ALE3D, Figure 8 shows that both dilation and rate effects affect ‘static strength.’ Once again, ‘static’ test simulations are explicit with $\dot{\epsilon} \approx 0.14 \frac{1}{s}$.

The moderate amount of strengthening that remains when the rate table is taken out is likely due to some inertial confinement mixed with structural confinement effects seen in Figure 4. Most interesting is the increasingly brittle response of the concrete specimen when first the rate table, then the dilation, is removed from the model. Without a rate

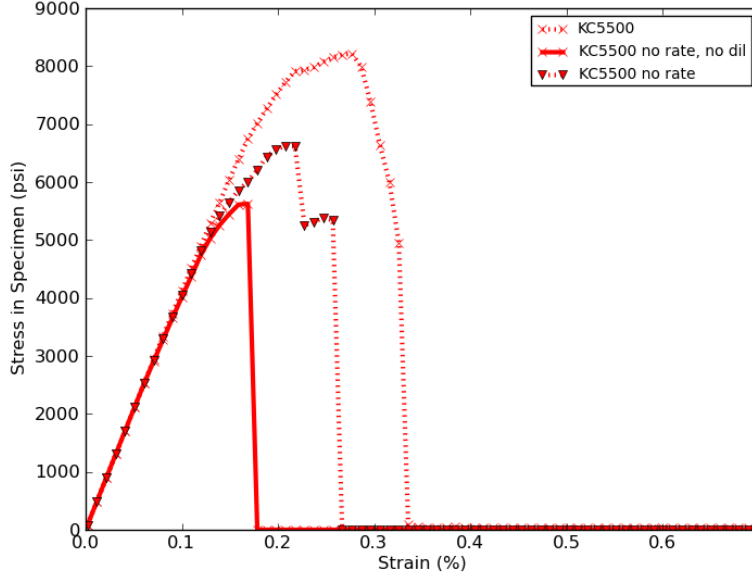


Fig. 8. Quasi-static tests on variants of the KC5500 model.

table, but with dilation, the softening response pauses at a plateau before proceeding rapidly to zero strength.

One trace in Figure 8 shows what happens when dilation is removed from the K&C model. Recalling equation 2.3, the dilation may be turned off by setting the ω_0 parameter equal to zero. Continuing the observation of various modifications to the dilation component of plastic flow: Table 4 describes the changes in the K&C model that were made to either turn off dilation, increase its contribution, or allow dilation to continue unabated by the damage process (i.e., set $m = 0$).

Table 4

Material Model Variations Regarding Dilation; $f'_c = 5500$, no rate table applied

Material Model Tag	Material Model Description	
KC5500 no rate, no dil	K&C ALE3D model without dilation	$\omega_0 = 0$
KC5500 no rate, unabated dil	Dilation does not degrade with damage	$\omega_0 = 0.5, m = 0$
KC5500 no rate, large dil	Fully associative flow	$\omega_0 = 1.0, m = 1,$

The large effect dilation has on the dynamic strength increase factor is plotted in Figure 9. Each of these DIF curves were normalized by the same static strength; that of ‘KC5500 no rate.’ Figure 9 shows that dilation accounts for most of the strength increase seen in the K&C ALE3D material model, and that turning off the decay of dilation after peak strength is attained will aid in strength increase, especially at very high strain rates.

When dilation is turned off, however, strength increase continues to occur. We shall see this indicates that there is a different flow rule at work between the K&C materials in different codes. The difference most likely centers on the implementation of the

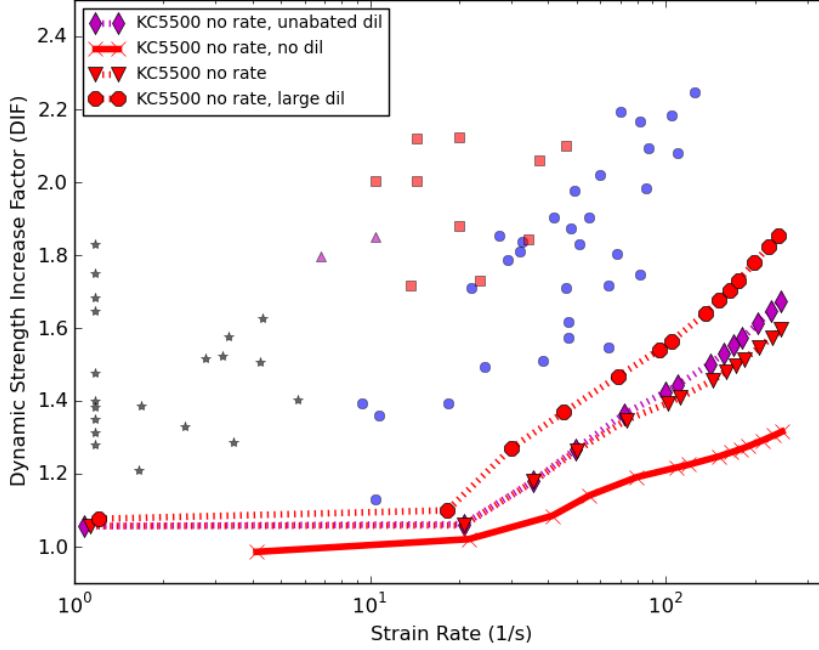


Fig. 9. Dilation's effect on dynamic strength increase for KC5500. Various effects of dilation outlasting damage ($m = 0$), fully associative flow ($\omega_0 = 1, m = 1$), and no dilation.

numerical derivatives eventually relating to the damage increment. In the longitudinally non-symmetrical event of a SHPB test, dilation properties of the material near the shear faults affect the core's ability to transfer load from the incident bar to the receiver.

Specimens subjected to a higher impact velocity that are comprised of DYNA3D materials not shown gaining strength, and the ALE3D K&C model without dilation, do not form the shear cone on the incident side of the specimen in the way a static experiment would. The failed portion of the specimen near the incident bar acts like a very compliant block of material, nearly equivalent to a frictionless test apparatus. The remaining undamaged specimen does not have friction derived confinement, which partially explains the loss of strength. The breakdown in strength gain is therefore partly a structural confinement effect. But, as shown in Figure 10, it is also a dynamic confinement effect and one that depends on the plasticity algorithm.

Figure 10 is a schematic illustration of the novel proposed mechanism at work in materials where dilation is allowed to continue to some extent throughout the damage process. Volumetric expansion confines shear strain occurring on the fault regions (observed in the static specimen in Figure 4). The shear forces are shown here as arrows; regions of volumetric expansion are shown as grey ovals on either side of the fault. In reality, the entire region is one localization zone. The inertia forces provided by the grey ovals of expanding material are also shown as arrows perpendicular to the shear cone (shown as a thin line). The figure is only representational of the process taking place to greater or lesser extent throughout the geometry. Simplified models (e.g. single element models) cannot accu-

rately capture this distribution, which is what makes a detailed computational model so useful. Volumetric expansion and the related preservation and confinement of the shear cone also take place on the cone nearest the receiver bar, although not shown in the figure.

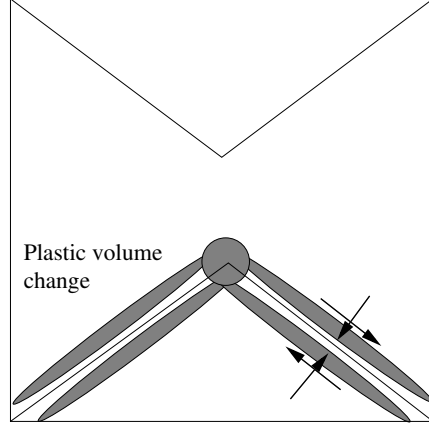


Fig. 10. Schematic representing the mechanism by which plastic volume change adds confinement on shear faults in the specimen. The dilating material provides confinement to the conic section.

Other factors like the quick generation and coalescence of cracks must also play a role in the extremely high strain rate regime, but are not captured by the present constitutive models. It has been observed by Malvern and coworkers [25] that the character of cracking within a specimen changes as the test's strain rate increases. Specifically, cracks in quasi-static tests are typically wider, less numerous and aligned with the load. The same cracks then become more numerous, their normals less aligned in the plane of tensile splitting and less capable of coalescing into a single specimen rupturing crack when the strain rate increases. The damage density increases and becomes more homogenized with increased strain rate.

Dilation is an implicit acknowledgement of extensive microcracking as volume gain cannot occur without aggregate first separating from the mortar. Given what has been shown, perhaps the best way to approach the correct DIF with a phenomenological plasticity model would be to *make dilation strain rate dependant* instead of the yield strength. Unfortunately, no such observations have been made of the dynamic dilation evolution response as a function of strain rate to correlate with simulation results. The dilation is likely to be highly dependant on location within a test specimen, which complicates such an effort.

Varying $\omega_0(\dot{\epsilon})$ from 0.5 to a value possibly in excess of 1.0 could account for all observed dynamic strength increase in compression. As we shall see in §3.10, element-by-element strain rates are typically orders of magnitude above what was recorded by the SHPB. Any such relationship, therefore, should not use abscissa values from SHPB tests. Effects related to the inertia of cracks or transient stress intensity fields generated by running cracks in the brittle medium could also be needed in a new phenomenological model. Existing 'smeared cracking' models usually have a poor treatment of plasticity and the shear dilation mechanism. Furthermore, sub element scales would need to be considered and multiscale modeling is expensive.

3.8. Code Verification Studies

Additional simulations were performed in DYNA3D and ALE3D to study behavior differences between the implementation of the material models across codes. Table 5 lists the two additional material models that were considered to check the code equivalence.

Table 5
Material Variations focused on DYNA3D vs. ALE3D, no rate tables

Material Model Tag	Material Model Description
KC-ALE3D-MAT65	K&C ALE3D model given material deck automatically generated from DYNA3D material type 65
DYNA-MAT45 Parameters from 65	DYNA3D material type 45 with input deck from automatically generated DYNA3D material type 65

Considering a few additional variations in the DYNA3D material models highlights some of the behavior differences between the two formulations and illustrates that material responses predicted by different vintages of K&C models are not perfectly equivalent. The DYNA3D material variants plotted in Figure 11 show a strong correlation between the DYNA K&C model (no rate table included) and the KC-ALE3D-MAT65. Other differences between the codes, such as contact algorithms, hourglass control, and operator splitting may be contributing to the minor difference in strain rate behavior. See [6] for more study of topics like hourglass control.

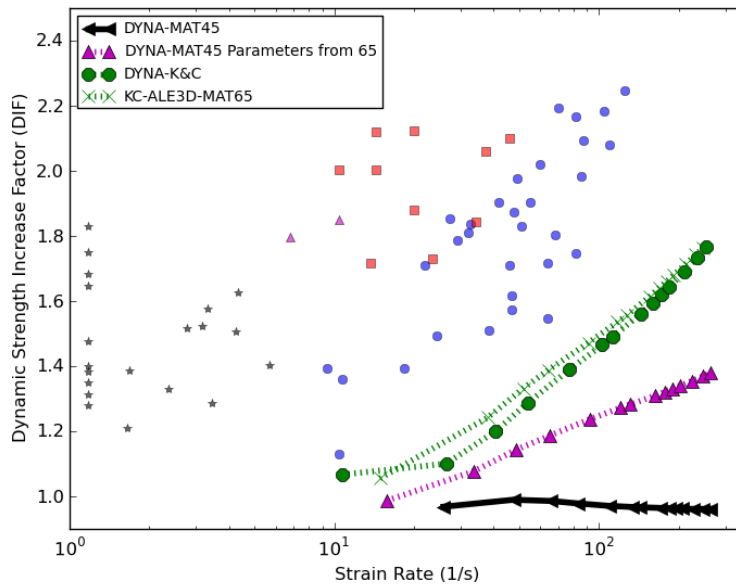


Fig. 11. Variants of the DYNA3D material model and comparisons to K&C ALE3D models

The two green lines in Figure 11 are quite similar, despite originating in different simulation codes. Both materials have the exact same input variable values. The auto-

matically generated parameters from DYNA K&C were directly input to the ALE3D simulation. The same parameters were input to “DYNA–MAT45 Parameters from 65” to check the algorithmic differences between those material models. The previous observations about damage affecting shear dilation (from equation 2.4) are likely the cause for the divergence. DYNA3D material 45, given the DYNA3D K&C model’s parameters, is more ductile but *eliminates* shear dilation after *damage* (not specific volume gain). The fact that dilation persists for a larger effective plastic strain in DYNA-K&C accounts for the observations in Figure 11.

Post peak *relative volume* maximums in these experiments are around 1.2. The denominator of equation 2.4 (the strain dilation adjustment) is only 1.016 for the K&C material and dilation is still active. Material 45, however, has completed the damage process in most load bearing portions of the specimen and dilation therefore does not continue, which leads to its lessened ability for strength gain.

3.9. Specimen Images of the Plastic Structural Mechanism: Plotting Dynamic Strength Increase from Dilation Response

The following section presents visual evidence of the dilation-based mechanism proposed in the previous section and sketched in Figure 10. The following figures show snapshots of the quarter round specimen from the SHPB test. Each specimen is from a test with increasing striker bar impact velocity (corresponding to Table 1), starting at the upper left and working left to right from the top to bottom row. The specimen is oriented to show the failure cone development on the interior. The incident pulse enters the specimen from the bottom and leaves through the top. To attempt absolute parity for comparison, each image is taken at the same time, regardless of the bar impact velocity or material model considered. This time is two microseconds after a survey of several SHPB analyses indicated the peak stress has passed. It is a snapshot in time of irreversible deformation processes that result during peak stress carrying capacity, but is taken before additional damage and deformation have taken place. Figure 12 shows the results for KC5500, which incorporates a rate table.

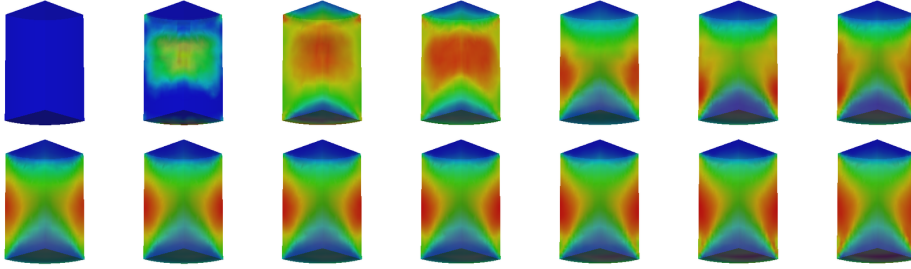


Fig. 12. Shear dilation with increasing striker velocity (left to right) for KC5500, $2 \mu s$ after peak stress as calculated by consensus from SHPB. Note that a different range is used for each color map to highlight the dilation pattern at each strain rate.

Dilation in the outer shear cone concrete is clearly visible in Figure 12. The magnitude of this dilation is also increasing. The maximum values (red) for each impact velocity are different and are determined by the maximum value for the particular problem. The color

map is not consistent, so that the pattern of dilation can be shown at each increasing strain rate. For the absolute maximum at each strain rate, see Figure 15.

When a rate table is used, the dilation has a tendency to collect in the jacket material around the core of the specimen. This supports core material with the momentum mobilized by plastic bulking because the jacket pushes inward on the core, providing confinement. Some of the patterns pictured in Figure 12 display a propensity to concentrate near the incident pulse (bottom of the specimen). The specimen in the lower right corner (highest impact velocity test) shows a moderate concentration of dilation on the shear faults. The situation is different when strain rate table enhancement is turned off, as shown in Figure 13.

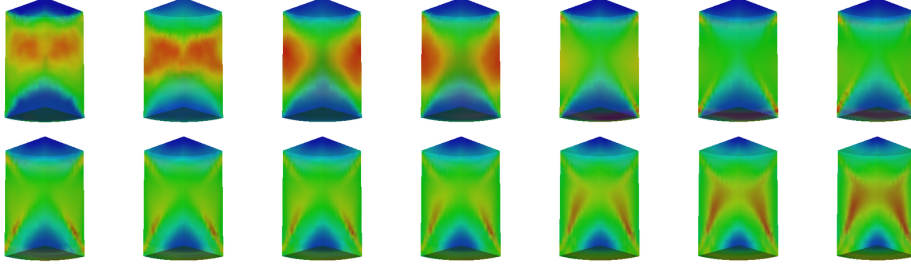


Fig. 13. Shear dilation with increasing striker velocity (left to right) for KC5500 with no rate table, $2 \mu\text{s}$ after peak stress. Note that a different range is used for each color map to highlight the dilation pattern at each strain rate

Without rate enhancement to support abnormal states of stress elsewhere in the specimen, the bulking occurring on the shear cones alone must provide for the additional strength. Note the similarity of the lower rates (upper left) of Figure 13 to some of the higher rate tests shown in Figure 12. The ‘jacket’ style bulking confinement is still taking place throughout the tests performed without rate enhancement, but without rate enhancement the shear faults will localize. Dilation becomes acute in areas bordering the shear cone, particularly near the exterior. Very small red portions can be seen in the upper right three sub-figures, c.f. Figure 13. Dilation in Figure 13 may have localized beyond the limit that would naturally be interrupted by aggregate. Multiple shear cracks between aggregate particles are seen in the two dimensional mesoscale models of Hao [13]. Including aggregate in the simulation leads to an increased DIF, since more shear faults occur and mortar material can still dilate and confine interaggregate failure planes.

The concentration of dilation strains near the exterior of the specimen may also appear to move into the core and disburse because the damage process has progressed faster under the more extreme loading that characterizes the lower right set of snapshots. The effect is still one and the same: Dilation begins on the outer, widest radius of the shear cone, then localizes on the shear faults and works toward the core. Jacket material supports the dilation for as long as possible before failing. The jacket material is made stronger by the use of a rate table, and with such a strength aid, the dilation doesn’t localize on the shear fault.

Figure 14 is a set of two material tests shown side-by-side. The set on the left has fully associative flow, resulting in more dilation, while the set on the right does not decrease dilation with damage. Figure 14 indicates that the largest shear dilation will

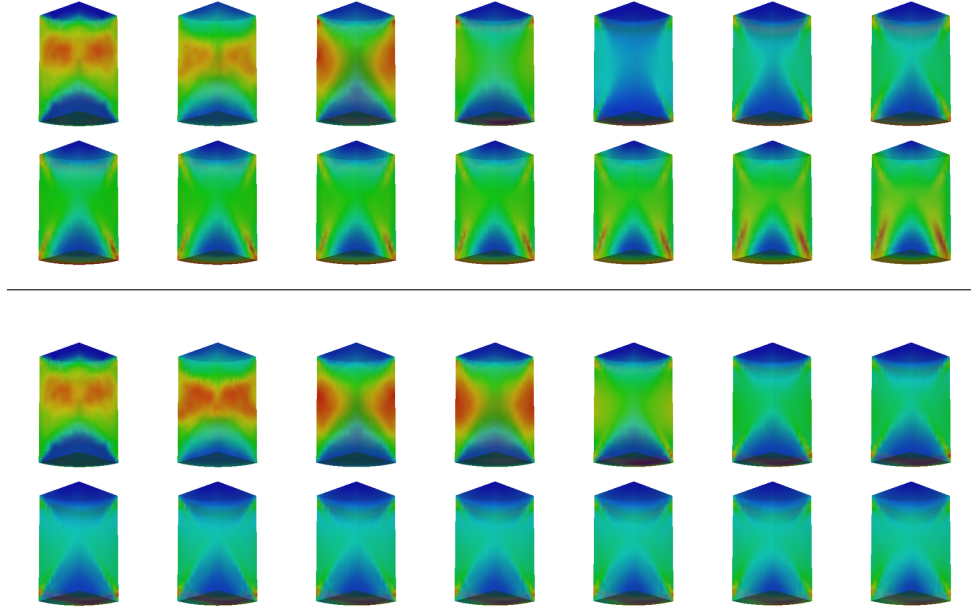


Fig. 14. Shear dilation with increasing striker velocity (left to right) for KC5500 with no rate table input; large (above) and unabated (below) dilation, $2 \mu\text{s}$ after peak stress as calculated by SHPB. Note that a different range is used for each color map to highlight the dilation pattern at each strain rate.

move towards the core if the damage process eliminates dilation on the exterior. The right subset of images in Figure 14 shows very small concentrated hotspots when the dilation process is unabated by damage. The dilation occurring in the shear bands is shown in stark relief when it is allowed to be fully associated with the plasticity algorithm.

Figure 15 displays the ‘meaning’ of the reddest color for each of the aforementioned plots. It shows that the magnitude of the maximum dilation in the specimen is significantly lower for the rate table enhanced material. Eliminating the artificial dependence of yield on strain rate serves to increase the maximum dilation. The final two modifications, where the dilation is fully associative or the damage is turned off, dramatically increase the maximum dilation value. Only the ‘large dil’ scenario results in significantly more strength increase because the additional dilation is spread out over the failure cones (c.f. Figure 14) instead of being concentrated in a small area on the exterior.

Figure 13 shows that without rate table enhancement, shear dilation occurs in regions more concentrated on the shear cone fault. There it serves to rapidly expand material on either side of the faults, thereby confining them. This action can be seen more prominently on the faults nearest the incident pulse, but also to a limited extent near the receiver bar. The strength increase mechanism changes from an overall jacketed type (inertial) confinement in the four lowest strain rates, to one more prominently featuring the X shape where dilation concentrates. As strain rates increase from moderate to severe levels, the dilation moves toward the core area.

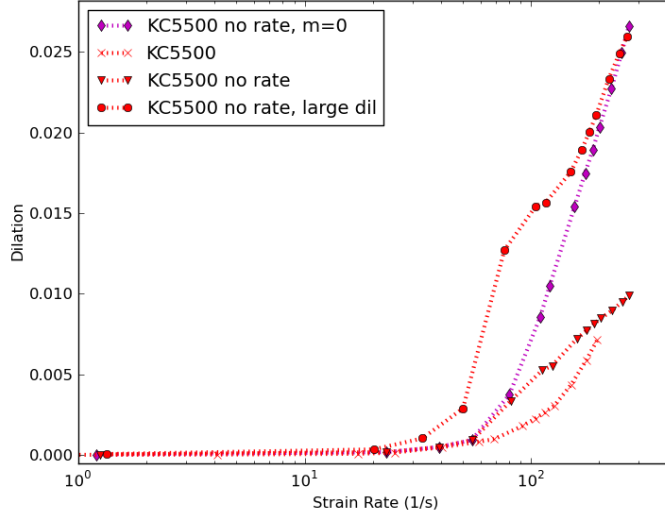


Fig. 15. Maximum dilation values at each strain rate

3.10. Strain Rate Pattern in SHPB Test Specimens

The dilation occurring in the specimen is accompanied by high strain rates in elements near the failure cone. Figure 16 shows the highest strain rates in the jacket material. For very fast striker impacts, the strain rates concentrate in elements near the ‘corners’ (upper radial periphery) of the test specimen. Figure 17 shows the maximum strain rates nearer the shear fault surfaces if rate tables are not employed. Figure 18 shows that the

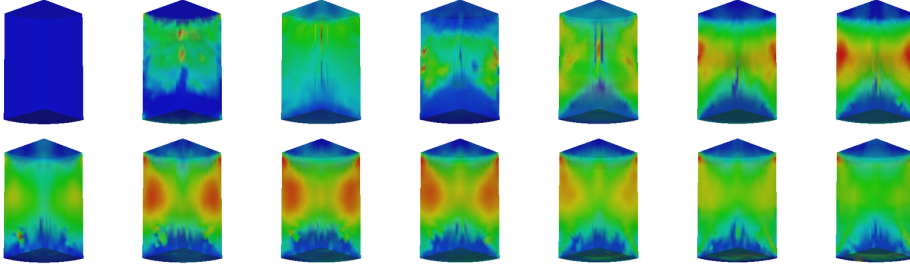


Fig. 16. Effective strain rate patterns with increasing striker velocity (left to right) for KC5500, $2 \mu\text{s}$ after consensus peak stress

maximum strain rates experienced anywhere in the specimen is higher when the material is not protected by a strain rate dependent yield strength table. However, even when the table is employed, maximum element strain rates can exceed the final tabulated abscissa of $1000 \text{ (1/s}^{-1}\text{)}$. Using a large dilation ω_0 coefficient and no rate table can drive the strain rates in a given element at three times that value. Without a strain rate table to scale the yield surface, the only ramification is the mobilization of a large amount of inertia during material expansion. It has been shown that this material motion produces

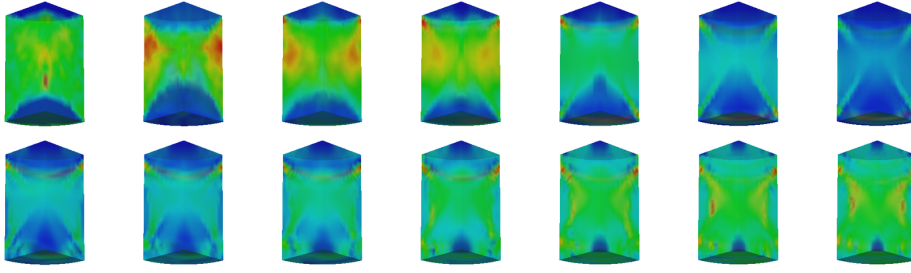


Fig. 17. Effective strain rate patterns with increasing striker velocity (left to right) for KC5500 with no rate table, $2 \mu\text{s}$ after consensus peak stress

the ‘dynamic confinement’ of interest, but it does not act in the most straightforward manner.

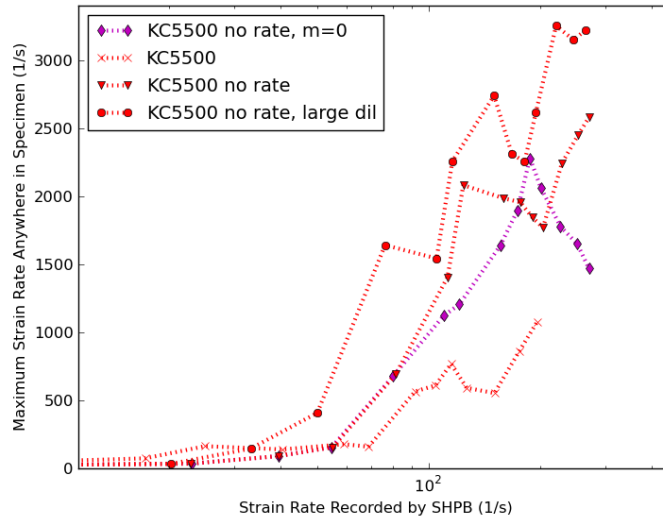


Fig. 18. Maximum element strain rate achieved anywhere in the specimen at each SHPB measured strain rate

4. Summary and Conclusion

The results presented show that dilation is a major factor in the dynamic strength increase of concrete materials loaded in compression. Dilation redirects local material point plastic flow away from what is dictated solely by the deviatoric stress state. Dilation mobilizes the inertia forces responsible for dynamic increase because expanding material on the local shear failure cone confines and strengthens the failing portion of the specimen structure. Pressure sensitivity is shown as a necessary, but not sufficient, condition for dynamic strength increase. The sensitivity to pressure must be exploited in the proper way by correct plastic flow and the damage process must not proceed too quickly. Most

simulation work to date has passed over this point when utilizing a material model that had dilation by simple virtue of its pressure sensitivity and associative flow rule.

Recommendations were made that the (somewhat arbitrary) proportion of plastic flow channeled into dilation be altered as a function of strain rate. This mimics the sub-element scale phenomenon of microcracking that is the cause of material dilation. The qualitative observation that microcracking is more prolific at high strain rates can be incorporated into the phenomenological plastic processes of the model. Properly calibrated, this mechanism could fully explain compressive dynamic increase. It would do so without violating the previously established 50% correlation of dilation to plastic flow observed in quasi-static tests. Dynamic experiments could conceivably be devised to validate this computational assumption. It has been shown that ceasing the dilation when damage occurs is a good aspect of the model as long as it is not done too soon. If not eventually stopped, dilation accumulates in select areas instead of spreading to locations where it has a stronger overall effect on the specimen (or larger system) strength.

Further investigations of dilation's role in strength increase are needed for problems like penetration and perforation. Since there is little quantitative data on the strength increase properties, there is a tenuous reliance on what are assumed to be 'material' properties, like yield surface scaling. This practice has been suspect in finite element analyses of complex systems under rapidly applied load. Dynamic strength increase in tension, where the practice may be justified for lack of a more suitable approach, is another large open question from a material modeling standpoint. Further development of phenomenological plasticity models for concrete should focus on the dilation mechanism for strength gain in compression, while relying on yield scaling functions for tensile increase.

4.1. *Auspices and Acknowledgements*

The authors would like to acknowledge the support provided by the National Science Foundation under Grant No. CMMI 0547670 for this work. Portions of this work were performed under the auspices of the United States Department of Energy by Lawrence Livermore National Laboratory under Contract DE-AC52-07NA27344 and funded by the Department of Homeland Security's Science and Technology Directorate.

References

- [1] A. Anderson, R. Cooper, R. Neely, A. Nichols, R. Sharp, and B. Wallin. Users manual for ALE3D an arbitrary Lagrange/Eulerian 3D code system. *LLNL, Version*, 3(1), 2003.
- [2] P.H. Bischoff and S.H. Perry. Compressive behaviour of concrete at high strain rates. *Materials and Structures*, 24(6):425–450, 1991.
- [3] CEB. *CEB-FIP Model Code 1990, Final Draft (Information Bulletin No. 195)*. Comité Euro-International du Béton (CEB), Lausanne, March 1990.
- [4] C. Chree. The equations of an isotropic elastic solid in polar and cylindrical coordinates, their solutions and applications. *Transactions of the Cambridge Philosophical Society*, 14:250–369, 1889.
- [5] JE Crawford and LJ Malvar. User's and theoretical manual for K&C concrete model. *Karagozian & Case, Burbank, CA, TR-97-53.1*, 1997.
- [6] W. Elmer VII. *Computational methods for simulation of extreme events on concrete structures*. Ph.d. dissertation, Univeristy of California Los Angeles, 2009.
- [7] P.S. Follansbee and C. Frantz. Wave propagation in the split Hopkinson pressure bar. *Journal of Engineering Materials and Technology*, 105(1):61–66, 1983.

- [8] MJ Forrestal, TW Wright, and W. Chen. The effect of radial inertia on brittle samples during the split Hopkinson pressure bar test. *International Journal of Impact Engineering*, 34(3):405–411, 2007.
- [9] J.F. Georgin and J.M. Reynouard. Modeling of structures subjected to impact: Concrete behaviour under high strain rate. *Cement and Concrete Composites*, 25(1):131–143, 2003.
- [10] DL Grote, SW Park, and M. Zhou. Dynamic behavior of concrete at high strain rates and pressures: I. experimental characterization. *International Journal of Impact Engineering*, 25(9):869–886, 2001.
- [11] KO Hakalehto. The behaviour of rock under impulse loads. A study using the Hopkinson split bar method'. *CTA polytechnica Scandinavica, Chemistry including metallurgy series No*, 81, 1969.
- [12] J.O. Hallquist. Theoretical Manual for DYNA3D. Technical Report UCID-19401, Lawrence Livermore National Laboratory (LLNL), Livermore, CA, 1983.
- [13] Y. Hao, H. Hao, and Z.X. Li. Numerical Analysis of Lateral Inertial Confinement Effects on Impact Test of Concrete Compressive Material Properties. *International Journal of Protective Structures*, 1(1):145–168, 2010.
- [14] B. Hopkinson. A Method of Measuring the Pressure Produced in the Detonation of High Explosives or by the Impact of Bullets. *Philosophical Transactions of the Royal Society of London. Series A, Containing Papers of a Mathematical or Physical Character*, 213:437–456, 1914.
- [15] W. Janach. The role of bulking in brittle failure of rocks under rapid compression. In *International Journal of Rock Mechanics and Mining Sciences & Geomechanics Abstracts*, volume 13, pages 177–186. Elsevier, 1976.
- [16] D.J.O.O. Kim, K. Sirijaroonchai, S. El-Tawil, and A.E. Naaman. Numerical simulation of the Split Hopkinson Pressure Bar test technique for concrete under compression. *International Journal of Impact Engineering*, 37(2):141–149, 2010.
- [17] H. Kolsky. An Investigation of the Mechanical Properties of Materials at very High Rates of Loading. *Proceedings of the Physical Society Section B*, 62(11):676–700, 1949.
- [18] Q.M. Li, Y.B. Lu, and H. Meng. Further investigation on the dynamic compressive strength enhancement of concrete-like materials based on split Hopkinson pressure bar tests. Part II: Numerical simulations. *International Journal of Impact Engineering*, 36(12):1335–1345, 2009.
- [19] Q.M. Li and H. Meng. About the dynamic strength enhancement of concrete-like materials in a split Hopkinson pressure bar test. *International Journal of Solids and Structures*, 40(2):343–360, 2003.
- [20] Zywickz E. Lin, J.I. DYNA3D: A Nonlinear, Explicit, Three-Dimensional Finite Element Code for Solid and Structural Mechanics. User Manual. Technical Report UCRL-MA-107254, Lawrence Livermore National Laboratory (LLNL), Livermore, CA, 2008.
- [21] J.M. Magallanes, Y. Wu, L.J. Malvar, and J.E. Crawford. Recent Improvements to Release III of the K&C Concrete Model. 2010.
- [22] LJ Malvar, JE Crawford, and KB Morrill. K&C concrete material model Release III—Automated generation of material model input. *Karagozian and Case Structural Engineers, Technical Report TR-99-24.3*, 2000.
- [23] L.J. Malvar, J.E. Crawford, J.W. Wesevich, and D. Simons. A plasticity concrete material model for DYNA3D. *International Journal of Impact Engineering*, 19(9-10):847–873, 1997.
- [24] L.J. Malvar and C.A. Ross. Review of Strain Rate Effects for Concrete in Tension. *Materials Journal*, 95(6), 1998.
- [25] L.E. Malvern, D.A. Jenkins, and R.T. DeHoff. Rate and Confinement Effects on Cracking and Failure in Uniaxial Compression of Concrete. Technical Report DTIC Research Report ADA261164, Florida Univ., Gainesville, Dept. of Aerospace, Engineering Mechanics and Engineering Science, 1992.
- [26] L.E. Malvern and C.A. Ross. Dynamic Response of Concrete Structures. 1982-85, *AFOSR Contract No. FR9620-83-K*, 1985.
- [27] L.E. Malvern and C.A. Ross. Dynamic Response of Concrete and Concrete Structures. Technical report, University of Florida Gainesville, 1986.
- [28] C. Noble, E. Kokko, I. Darnell, T. Dunn, L. Hagler, and L. Leininger. Concrete Model Descriptions and Summary of Benchmark Studies for Blast Effects Simulations. Technical report, UCRL-TR-215024, Lawrence Livermore National Laboratory (LLNL), Livermore, CA, 2005.
- [29] L. Schwer. Strain rate induced strength enhancement in concrete: Much ado about Nothing? *Proc. Seventh European LS-DYNA Conference, May 14-15 Salzburg, Austria*, 2009.

- [30] J.C. Simo, J. Ju, K.S. Pister, and R.L. Taylor. Assessment of Cap Model: Consistent Return Algorithms and Rate-Dependent Extension. *Journal of Engineering Mechanics*, 114(2):191–218, 1988.
- [31] JW Tedesco, ML Hughes, and CA Ross. Numerical simulation of high strain rate concrete compression tests. *Computers & Structures*, 51(1):65–77, 1994.
- [32] J.W. Tedesco and C.A. Ross. Experimental and Numerical Analysis of High Strain Rate Splitting-Tensile Tests. *Materials Journal*, 90(2), 1993.
- [33] Z. Tu and Y. Lu. Evaluation of typical concrete material models used in hydrocodes for high dynamic response simulations. *International Journal of Impact Engineering*, 36(1):132–146, 2009.
- [34] M. Zhang, H.J. Wu, Q.M. Li, and F.L. Huang. Further investigation on the dynamic compressive strength enhancement of concrete-like materials based on split Hopkinson pressure bar tests. Part I: Experiments. *International Journal of Impact Engineering*, 36(12):1327–1334, 2009.
- [35] XQ Zhou and H. Hao. Modelling of compressive behaviour of concrete-like materials at high strain rate. *International Journal of Solids and Structures*, 45(17):4648–4661, 2008.